01,08,16

Size-dependent optical properties of aluminum nanoparticle arrays formed by vacuum-thermal deposition

© O.P. Gorelkov, L.S. Volkova, T.S. Grishin, A.O. Kozlov, A.Yu. Trifonov, A.V. Pavlikov, I.V. Lavrov, S.V. Dubkov, A.V. Anikin, D.G. Gromov

Federal State Autonomous Education Institution of Higher Education
National Research University „Moscow Institute of Electronic Technology“,
Moscow, Zelenograd, Russia

E-mail: oleg.gorelkov@gmail.com

Received August 15, 2025
Revised August 15, 2025
Accepted August 28, 2025

The processes of aluminum nanoparticle (Al-NPs) array formation by vacuum-thermal evaporation and condensation at a substrate temperature of 150 °C were studied using SEM, TEM and ellipsometry methods. It was shown that the particles in the array have a flattened shape, and their average size in the array depends linearly on the amount of deposited aluminum. Experimental spectral dependences of the refractive index, extinction coefficients and transmittance of Al arrays coated with a SiO_2 layer were obtained. Experimental data were compared with the results of modeling the Al-NPs/SiO_2 composite material using the Maxwell–Garnett approximation and its generalization. It is shown that an important factor determining the spectral optical characteristics of the Al-NPs/SiO_2, composite material is the non-uniformity of Al nanoparticle shape in the array.

Keywords: plasmon resonance, aluminum, nanoparticles, electron beam evaporation, ellipsometry, optical properties.

DOI: 10.61011/PSS.2025.09.62346.231-25

1. Introduction

Metal nanoparticles facilitate origination of localized surface plasmonic resonances (LSPR) due to coherent collective oscillations of their surface conductance electrons [1]. With optical stimulation at a resonance frequency, the LSPR generates a highly-localized and intense electromagnetic field near the nanoparticle [2].

This phenomenon provides considerable absorption and scattering of light by the nanoparticles. Resonance characteristics, including a frequency and a line width, depend on a material composition, a geometrical form and a refractive index of the environment [2]. As a result, the nanoparticles demonstrate exceptional nanooptical properties that are useful for various process applications. They include supersensitive probing, surface-enhanced Raman spectroscopy (SERS) [3–5], metal-enhanced fluorescence and photocatalysis [1,2,6–10].

The LSPR phenomenon was extensively studied in nanoparticles of noble metals, in particular, gold and silver, which have been main materials for research for a long time [1,11]. They dominate in this field due to a combination of unique optical, chemical and physical properties. The gold and silver nanoparticles demonstrate strong, clearly pronounced LSPR peaks in the spectrum from visible to near-infrared (400–1000 nm) radiation. This range is crucial for many photonic and biological applications [1,12,13], since it coincides with operating wavelengths of usual lasers, optical detectors and microscopic systems. Moreover, gold has high chemical inertia and is resistant to oxidation and corrosion even in the environmental conditions, thereby providing long-term stability of plasmon nanostructures [14].

Although gold and silver are still fundamental materials in plasmonics, the latest achievements have underlined a potential of aluminum due to its plasmon activity in the ultraviolet spectrum. Besides, aluminum is a more common, economically profitable material which is compatible with modern technologies of semiconductor production [15]. One of the key advantages of aluminum is its capability of maintaining strong plasmon resonances at the shorter wavelengths (up to 250 nm), where traditional plasmon metals, such as gold and silver, are less effective [11,15]. Besides, the aluminum nanoparticles demonstrate variability of an LSPR position, which depends on a particle size, their form and oxidation degree, thereby providing flexibility when designing the plasmon devices [2]. Aluminum can be very easily oxidized in air atmosphere and forms a oxide film of the thickness of about 2 nm on its surface [16]. It was shown that when varying the content of the aluminum oxide one can attain changing of plasmon reactions [16]. This makes this material suitable for application in sensorics, catalysis and photonics.

Thus, all these properties taken together underline the potential of aluminum as a stable and adaptable material for designing the next-generation plasmon systems for such fields as biomedical diagnostics [12], integral photon circuits [17], nonlinear optics, lasers, photoluminescence, sensors on an aluminum metal film [15].

Yet another promising application of the plasmon nanostructures is plasmon lithography. It was noted in some

articles that this method of obtaining images on a photoresist film made it possible to produces structures with sizes of below 10 nm and furthermore it is a more economically-profitable as compared to other types of lithographic processes [18,19]. In this regard, aluminum is also interesting as a plasmon material. It was shown that the aluminum plasmon nanostructures made it possible to obtain a highly-contrast image in the photoresist with the size $\lambda/6$ [20].

Currently, a lot of methods of production of the LSPR structures are studied. For example, it includes various lithography methods: nanosphere lithography, nanoimprint lithography, holographic lithography and direct-write lithography [21]. These methods make it possible to obtain a quite accurate arrangement of arrays with a small number of defects on the substrate surface. But a main disadvantage of these methods is their high cost and a necessity of overcoming a diffraction limit to produce the small-sized particles. The literature also mentions colloidal methods [22]. They allow producing the small-sized particles, but they are small-scaled, require using stabilizing substances and it is also difficult to purify a finished product from substances used during their production.

The most economically-profitable and technologically simple methods of producing the nanoparticle arrays are various methods of deposition from a vapor phase, for example, deposition at an oblique angle [23], vacuum-thermal sputtering [24–26].Due to vacuuming during the production process, they allow producing the arrays that consist of particles of a quite small size and a high purity degree.

In the present study, we demonstrate that it is possible to controllably produce the aluminum nanoparticle arrays by vacuum-thermal evaporation and the optical properties of the produced arrays. Thus, the present article is aimed at experimental and theoretical characterization of the optical properties of the aluminum nanoparticle arrays produced by vacuum-thermal deposition, in a dependence on the sizes and the form of the nanoparticles.

2. Methods of producing and investigating the samples

2.1. Formation of the aluminum nanoparticle arrays

Various substrates were used when manufacturing the samples: quartz glass — for studying the optical properties, silicon with a thermal oxide layer of the thickness of 300 nm — for studying by scanning electron microscopy (SEM) and amorphous carbon of the thickness of 20 nm — for studying by transmission electron microscopy (TEM). The Al nanoparticle arrays were formed on the said substrates by electron-beam evaporation in an installation Angstrom EvoVac-34 at the residual chamber pressure of at most $4 \cdot 10^{-8}$ Torr. The substrate were heated to the temperature of 150 °C, which was followed by cleaning the substrate surfaces with argon ion bombardment under the following conditions: a working gas pressure is 1.0 mTorr; a Ar flowrate is 4.8 cm^3/min; a processing time is 30 s. It was followed by a process of aluminum deposition at the rate of 0.3 Å/s. The aluminum layers of the thickness of 1.5, 3.0 and 4.5 nm were deposited for the studies. It should be noted that when depositing Al of such small thickness, thin films, as will be demonstrated, will just be the nanoparticle array and, therefore, the said film thicknesses are virtual. At the final stage, in a single vacuum cycle, the formed Al nanoparticle array was covered with a SiO_2 layer of the thickness of 7.5 nm by electron-beam evaporation, too (the deposition rate was 1 Å/s), to prevent oxidation of the Al nanoparticles during storage in air.

2.2. Investigation of the surface morphology of the aluminum nanoparticle arrays

The surface morphology, in particular, lateral geometrical sizes of the Al nanoparticle in the array were investigated using scanning electron microscopy. The samples were studied in a two-beam electron-ion microscope Helios G4CX (Thermo Fisher Scientific, USA) at the accelerating voltage of $HV = 5$ kV, the beam current of $I_e = 86$ pA and the working distance of $WD = 4$ mm. Secondary electron images were obtained by means of an in-lens detector in an immersion mode.

A focused ion beam (FIB) integrated into the electron-ion microscope Helios G4CX was used to prepare a thin cross section (lamella) of the sample with the Al nanoparticle array for subsequently studying the geometry of the cross section of the nanoparticles, in particular, their height, by transmission electron microscopy. In order to protect an interest area from unintentional destructive effect by the ion beam, a Pt protective layer was formed using a gas injection system integrated into the microscope. First of all, the Pt layer of the thickness of ~ 150 nm was deposited in conditions of electron-beam induction, which was followed by deposition in ion-beam conditions until reaching the total thickness of about $1-2\,\mu$m.

Then, the material was roughly locally removed at the accelerating voltage $HV = 30$ kV and the ion-beam current $I_i = 2.5$ nA to form a lamella blank. Formation of the lamella blank was followed by its pre-thinning using the same accelerating voltage (30 kV), but with the reduced ion-beam current (0.43 nA). Then the lamellas were extracted by means of a nanomanipulator (EasyLift), accurately transferred to a copper mesh for TEM and fixed by additional Pt deposition.

Final thinning and surface cleaning included gradual reduction of the accelerating voltage from 10 to 2 kV with a gradual decrease of the beam current to tens of picoamperes. This gentle staged approach to thinning made it possible to minimize ion-induced structural damage and amorphization effects, in particular, to remove a surface amorphized layer formed at the early stages of preparation and to achieve optimal electron transparency of a plate

Table 1. Information about the studied samples

Reference number of the sample	Description	Quantity ratio a virtual thickness	Substrate temperature during deposition
#1	Nanoparticles of Al, covered by SiO_2	Al 1.5 nm/SiO_2 7.5 nm	+150 °C
#2	Nanoparticles of Al, covered by SiO_2	Al 3.0 nm/SiO_2 7.5 nm	+150 °C
#3	Nanoparticles of Al, covered by SiO_2	Al 4.5 nm/SiO_2 7.5 nm	+150 °C

(of the thickness below 100 nm). At all the stages of preparation, quality control included high-resolution electron visualization using detectors of secondary (SE) and back-scattered (BSE) electrons in order to ensure structural integrity and precise sizes of the finished plate.

2.3. Investigation of the crystal structure of the al nanoparticles in the array

The crystal structure of the Al nanoparticles in the array and their cross section were studies by means of a transmission electron microscope Tecnai G^2 20 S-Twin (Thermo Fisher Scientific, USA), which was equipped with a energy-dispersive spectroscopy (EDS) system produced by EDAX. A chemical composition of the surface and valence states of the Al nanoparticles were determined using a photoelectron spectrometer PHI 5000 VersaProbe II with a monochromatized source of excitation by radiation Al K_α ($h\nu = 1486.6$ eV, the power is 50 W, the diameter is 200 μm).

The TEM method was used to study the samples with the Al nanoparticle array on amorphous carbon and the thin cross section prepared by FIB as noted above. An amorphous-carbon layer of the thickness of 20 nm was first formed on a NaCl salt crystal by magnetron sputtering. For the TEM studies, the thin amorphous-carbon layer with the Al nanoparticle array already formed thereon was separated from the NaCl crystal by immersing into deionized water and dissolving the latter and then displaced to the copper mesh for TEM.

2.4. Investigation of the optical properties of the aluminum nanoparticle arrays

A spectroscopic ellipsometer SER 850 DUV with a measurement range from 190 to 3500 nm was used to determine spectral dependences of the optical characteristics of the material. The ellipsometer is designed to study fine transparent films and layers and to obtain dependences of a relative phase difference Δ for s- and p-polarizations of an incident and reflected beam as well as a value of ψ that characterizes an amplitude ratio of these polarizations. When having the spectral dependences of Δ and ψ, one can determine thicknesses of the studied layers and the spectral dependences of a refractive index (n) and an extinction coefficient (k).

A spectrophotometer Agilent Cary 5000 was used to measure transmittance spectra within the wide spectral range from 180 nm to 3.3 μm due to availability of an additional PbSmart detector. The spectrophotometer is characterized by an extended photometric range and designed to measure absorbance above 8 within the entire spectral range from UV to IR. An additional attachment with an integrating sphere makes it possible to measure the spectra of reflection and scattering within the spectral range 180 nm – 1.8 μm.

3. Results and discussion

The studies were performed on the three samples of the aluminum nanoparticles. The characteristics of the samples are given in Table 1.

Figure 1 shows the SEM images of the surface of the studied samples under the same magnification. As can be seen, in all the cases the surface exhibits the nanoparticle arrays with the difference that when depositing the layer of the virtual thickness of 1.5 nm the array consists of a large number of fine nanoparticles, while depositing the thicker layer of the virtual thickness of 4.5 nm the array consists of a smaller number of the particles of a noticeably larger size. The obtained images were taken to determine the size distribution of the particles. The average size of the particles of the sample # 1 was 11.5 ± 1.7 nm, while that of the sample # 2 was 20.7 ± 7.0 nm, and that of the sample # 3 was 36.2 ± 11.9 nm.

Based on the obtained data, we have plotted the dependences of the average size of the particles (Figure 2, a) and the number of the particles (Figure 2, b) per the unit area on the virtual film thickness. The experimental values of the average size of the Al nanoparticles were approximated to a linear function by the least-square method to provide a correlation coefficient of 0.989 (Figure 2, a), thereby indicating a linear nature of the dependence of the average size of the nanoparticles on the virtual film thickness, i. e. actually, on the amount of condensed aluminum. At the same time, the values of the number of the Al particles in a dependence on the virtual film thickness (with the correlation coefficient of 0.998) are well approximated to

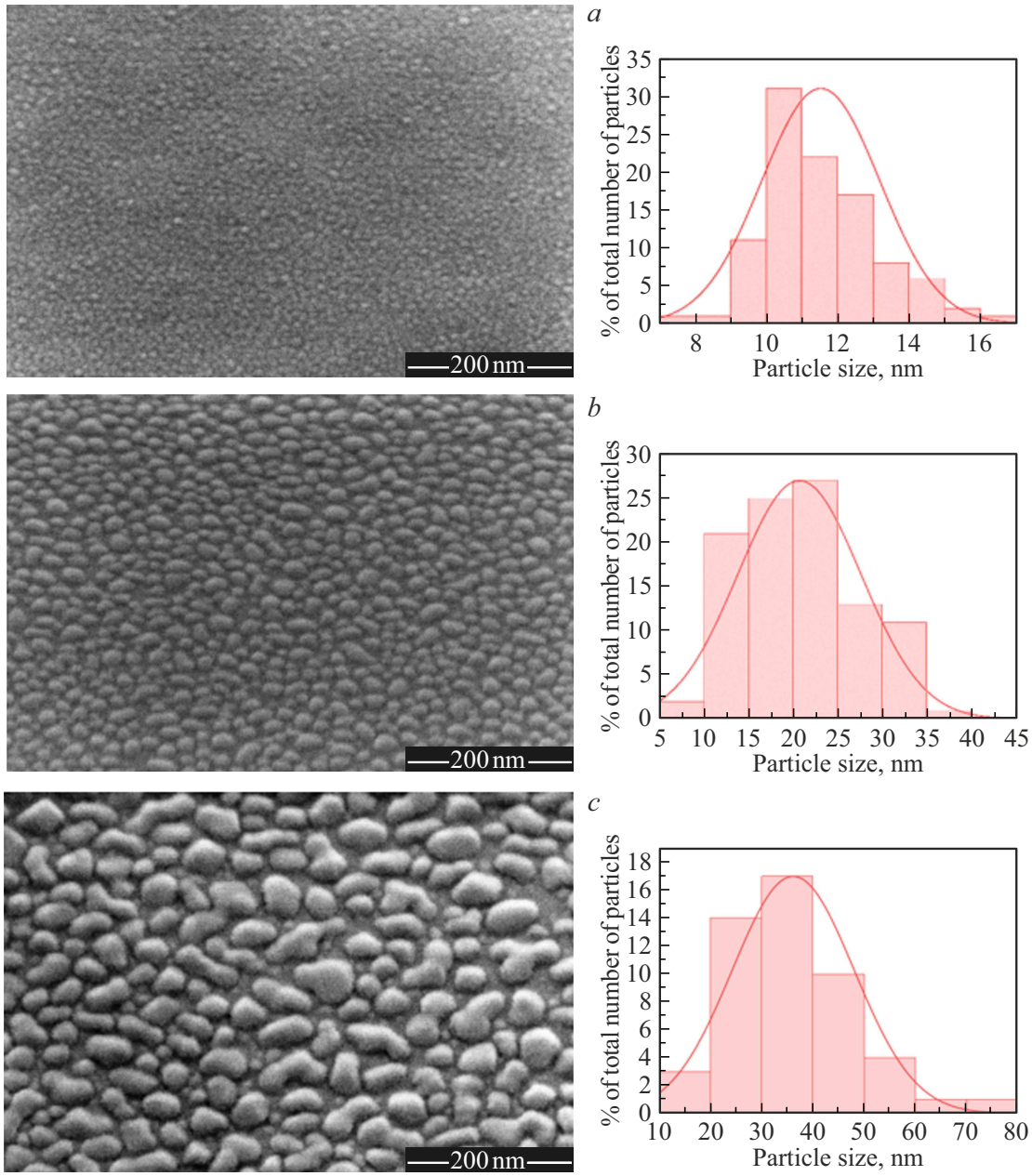

Figure 1. SEM-images under magnification ×600k (on the left) and histograms of aluminum-nanostructure size distribution of the particles (on the right) *a* — the sample #1; *b* — the sample #2; *c* — the sample #3.

an exponential function (see Figure 2, *b*). The obtained dependences of variation of the nanoparticle size and the number of the aluminum particles in the array are similar to those previously observed for the other materials, such as silver and gold [24,25]. It is obvious that the form of these patterns is of a general nature regardless of the material and is a key to control of parameters of the formed nanoparticle arrays when using vacuum-thermal evaporation.

Figure 3 shows results of the studies of the samples #2 and #3 by TEM. Contrasting TEM images of the Al nanoparticle array of the sample #1 could not be obtained. Therefore, it was impossible to determine their boundaries and, therefore, the sizes, which is obviously related to the too small thickness of the nanoparticles in this array and a small mass of the Al atoms at the same time. Even for the samples #2 and #3, which contained the substance in 2 and 3 times higher than in the sample #1, the contrast of the images in the usual TEM mode was very weak. Therefore, a small-diameter lens aperture was used when obtaining the images.

The obtained images were analyzed to make it also possible to plot the histograms of size distribution of the Al nanoparticles (Figure 3) and to determine the average size of the particles of the sample #2: 20.9 ± 4.9 nm

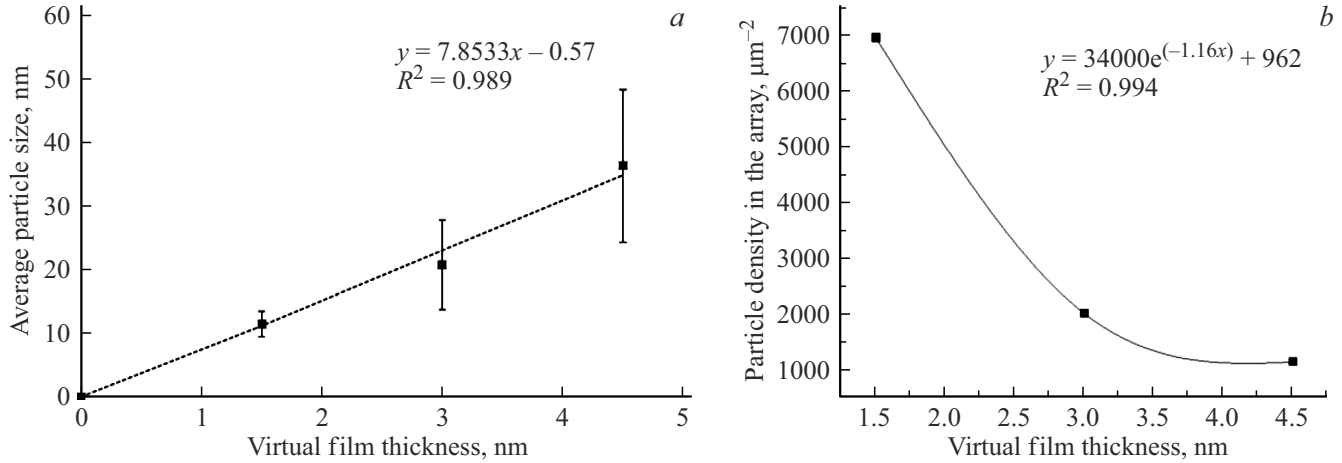

Figure 2. Dependences of an average size of the aluminum particles (*a*) and a number of the aluminum particles per an array unit area (*b*) on the virtual film thickness.

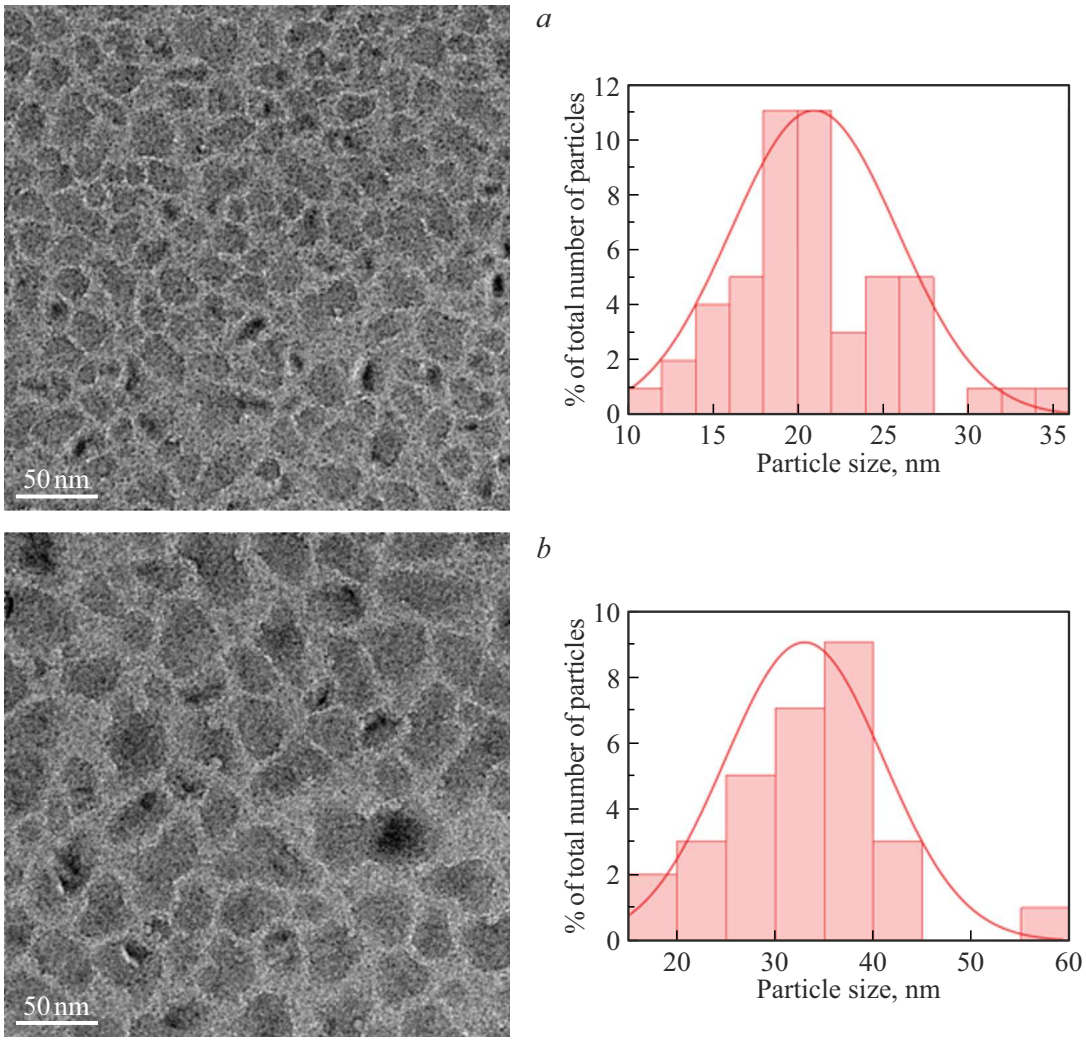

Figure 3. TEM-images under magnification ×71k (on the left) and histograms of aluminum-nanostructure size distribution of the particles (on the right): *a* — the sample #2; *b* — the sample #3.

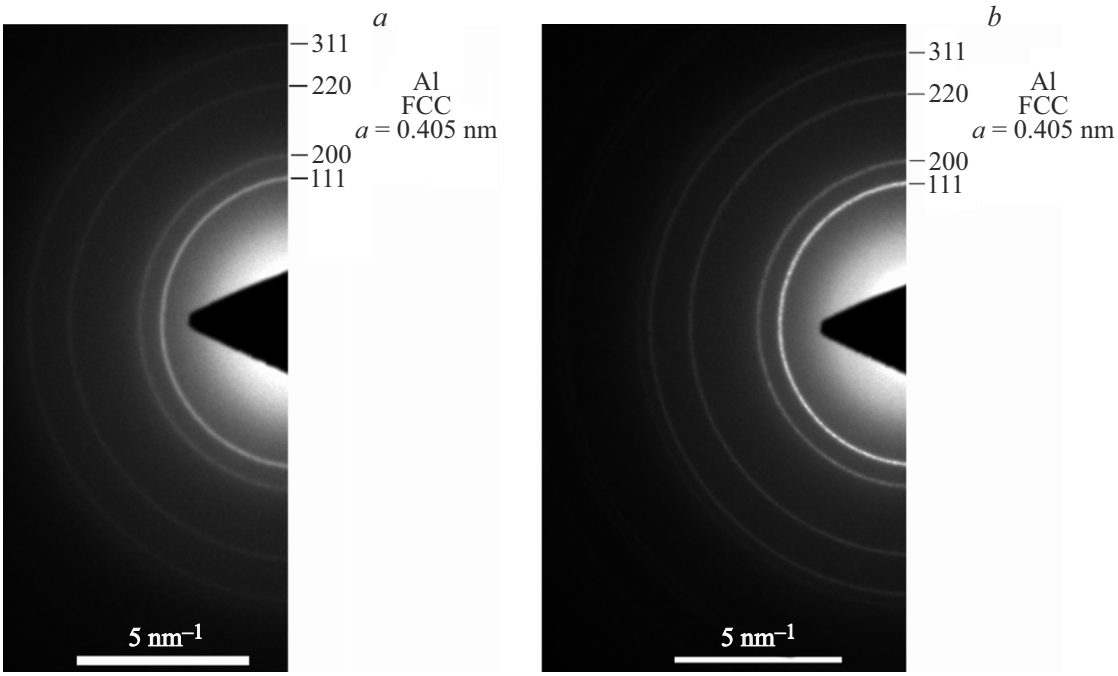

Figure 4. Selected area diffraction patters (SADP) of the aluminum nanostructures: *a* — the sample #2; *b* — the sample #3.

and the sample #3: 32.9 ± 8.1 nm. Although the Al nanoparticle arrays for TEM were formed on the surface of amorphous carbon, it can be seen that, nevertheless, the averages nanoparticle size of the respective samples #2 and #3, which is determined by the SEM- and TEM-images excellently coincides within the specified errors.

In order to determine a crystal state of the films, the selected area diffraction patterns (SADP) were obtained for both the samples. They are shown in Figure 4. The selected area was a circle of the diameter of about $1\,\mu$m. The diffraction patterns from both the samples are practically the same and correspond to a polycrystalline structure with an aluminum FCC lattice with a lattice parameter $a = 0.405$ nm.

Lattice planes in some nanoparticles can be observed at images that are obtained at large magnifications in a mode of high-resolution electron microscopy (HREM). For the sample #2, this image is shown in Figure 5. You can see in it an image of one nanoparticle oriented along a zone axis [110]. The insert also includes a Fourier transform of the presented image with indexed reflections of the lattice planes. The entire particle is a single aluminum single crystal.

Besides, TEM was used to study the manufactured thin cross section of the sample #2, which made it possible to specify side sizes of the aluminum nanoparticles in the array. A typical cross section of the aluminum particle is shown in Figure 6. As can be seen, a height of the nanoparticle is approximately in two times less than a planar size. Thus, the form of the aluminum nanoparticles is far from a spherical one. The images of the cross section of the various nanoparticles in the array were statistically analyzed to show that to ratio of the length to the height of the structures varies within the interval 1.9–2.5. At the same time, no correlation with the planar size was detected.

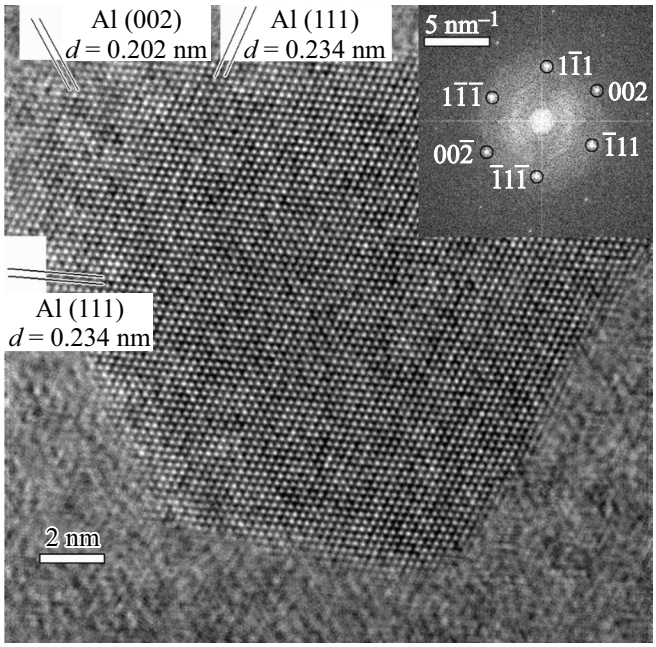

Figure 5. Images of the aluminum nanostructures of the sample #2 in the high-resolution mode (HREM) with magnification ×1050k, the zone axis [110]. The insert includes a diffraction pattern of the sample with indexed reflections from the planes of the aluminum FCC lattice.

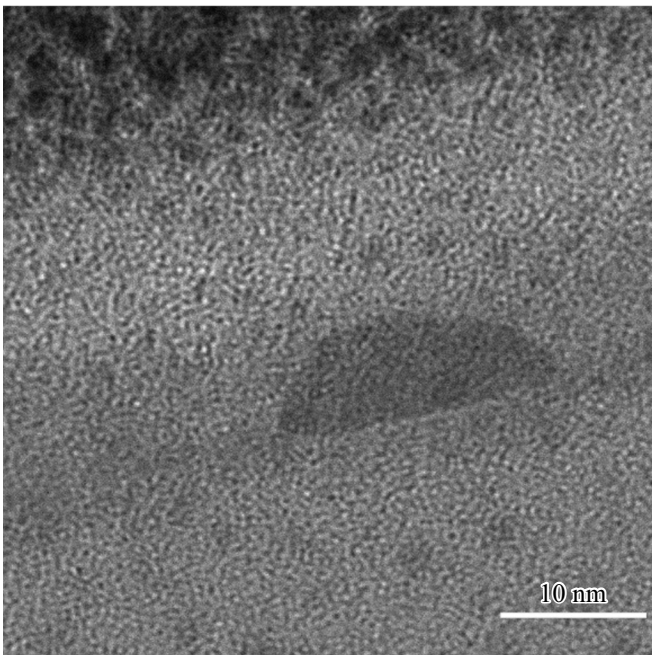

Figure 6. TEM images of the cross section of the sample #2.

The optical properties of the produced samples with the Al nanoparticle arrays in a combination with their covering SiO_2 layer were studied by means of ellipsometry. Figure 7 shows the spectral dependencies n and k of the studied samples of the aluminum nanoparticle arrays covered with the SiO_2 layer. The layer thicknesses determined by means of ellipsometry were 11.0 ± 0.5 nm for the sample #1, 13 ± 0.5 nm for the sample #2 and 14.5 ± 0.5 for the sample #3, respectively.

By comparing the presented dependences, one can note that n for all the samples monotonically increases within the spectral range from 190 to 600 nm. But the range of variation of n increases with an increase of the average size of the Al nanoparticles: from 1.4 to 1.7 for the sample #1, from 1.0 to 2.5 for the sample #2, from 0.5 to 3.4 for the sample #3.

The given dependences well correlate with the dependence k shown in Figure 7, *b*. It is clear in the figure that with an increase of the average size of the Al nanoparticles the extremum k is shifted towards the high wavelengths.

Layers' transmittance spectra T were also measured and are shown in Figure 8. It is clear from the presented spectra that with an insignificant increase of the thickness T noticeably decreases, while the minimum of transmittance is shifted into a red region, which complies with shifting of the position of the peak k.

In order to simulate the optical properties of the produced aluminum films, the sample #2 was selected. It is related to the fact that, as shown above, the optical properties of the studied samples have a qualitative similarity and vary regularly with the increase of the aluminum nanoparticle size and to the fact that a cross section was made for this sample, which made it possible to determine the transverse sizes of the Al nanoparticles along with its lateral sizes for it.

It was shown by the performed electron-microscopic studies that the produced samples of the Al nanoparticle arrays covered with the SiO_2 layers were essentially a composite film, i.e. it can be represented as a matrix composite, where the matrix is SiO_2, in which aluminum inclusions are immersed. At the same time, the very Al inclusions have quite flattened shapes and sizes of the inclusions in the film plane in several times exceed a size in a direction perpendicular to the film plane. There is also a quite considerable spread in ratios of the inclusion sizes in the film plane from approximately round to substantially elongated chains of the clumped inclusions with a various orientation in the film plane. The real form of the inclusions can be simulated by ellipsoids with various aspect ratios. Since the inclusion sizes and distances therebetween are significantly less than the length in the considered range $0.2-0.8\,\mu$m, then in order to predict

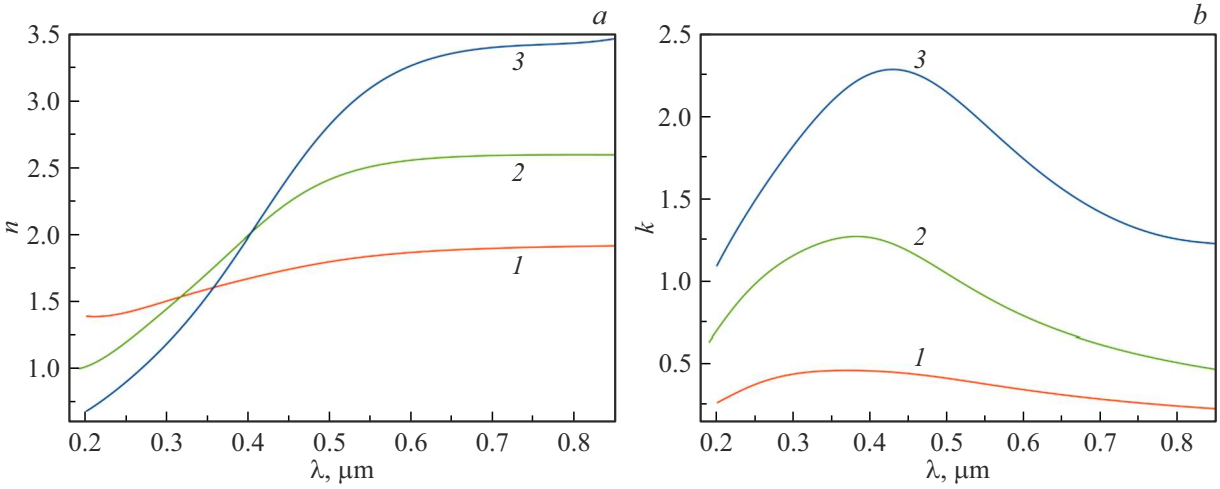

Figure 7. Dependences of the refractive index n (a) and the extinction coefficient k (b) of the samples #1, #2, #3 on the wavelength.

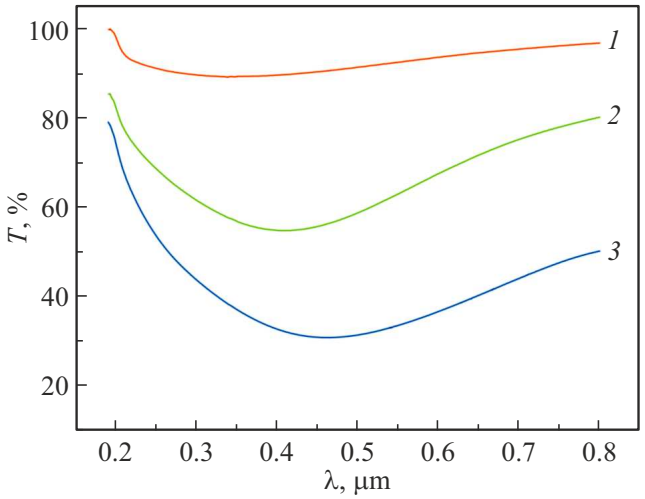

Figure 8. Variation of the transmittance factor of the produced samples # 1, # 2, # 3 in a dependence on the wavelength.

the optical characteristics of the composite a quasistatic approach can be applied. Since the magnetic properties of components of this heterogeneous medium are absent, then its optical properties are determined by effective permittivity as a function of a frequency of the affecting electromagnetic field.

The tensor $\boldsymbol{\varepsilon}^*$ of effective permittivity of the sample of the heterogeneous medium is determined by an equation $\langle \mathbf{D} \rangle = \boldsymbol{\varepsilon}^* \langle \mathbf{E} \rangle$, where $\langle \mathbf{D} \rangle$, $\langle \mathbf{E} \rangle$ are electrical inductance and strength of the electric field, respectively, that are averaged across the sample (it is assumed that an ergodicity hypothesis can be applied, i. e. an average across of an ensemble of implementations of the heterogeneous medium coincides with an average across the sample of the heterogeneous medium). The tensor $\boldsymbol{\varepsilon}^*$ of the matrix composite shall be calculated to predict its optical properties by using a Maxwell–Garnett (MG) approximation and its generalizations [27]. By taking into account the spread of forms and orientations of the inclusions, it is naturally possible to realized the following option of the generalized MG approximation, in which $\boldsymbol{\varepsilon}^*$ is calculated by the formula [28]:

$$\boldsymbol{\varepsilon}^* = [(1-f)\varepsilon_m \mathbf{I} + f\langle \boldsymbol{\kappa} \rangle][(1-f)\mathbf{I} + f\langle \boldsymbol{\lambda} \rangle]^{-1}, \quad (1)$$

where ε_m is permittivity of the matrix, f is a volume portion of all the inclusions in the material; $\mathbf{I}$ — a second-rank unit tensor; the second-rank tensors $\boldsymbol{\lambda}$ and $\boldsymbol{\kappa}$ are related to a specific inclusion and written as:

$$\boldsymbol{\lambda} = [\mathbf{I} + \varepsilon_m^{-1}\mathbf{L}(\boldsymbol{\varepsilon} - \varepsilon_m \mathbf{I})]^{-1}, \quad \boldsymbol{\kappa} = \boldsymbol{\varepsilon}\boldsymbol{\lambda}. \quad (2)$$

In the expressions (2), $\mathbf{L}$ is a tensor of geometrical factors of this ellipsoidal inclusions, $\boldsymbol{\varepsilon}$ is a tensor of permittivity of the inclusion. The main components of the tensor $\mathbf{L}$ are determined by the formulas [27]:

$$L_i = \frac{a_1 a_2 a_3}{2} \int_0^\infty \frac{du}{[a_i^2 + u]R_u}, \quad i = 1, 2, 3;$$

$$R_u = \left[(u + a_1^2)(u + a_2^2)(u + a_3^2)\right]^{1/2}, \quad (3)$$

where a_1, a_2, a_3 are ellipsoid semi-axes.

In (1), it is averaged along all the sample inclusions and it can take into account various types of the inclusions in terms of material properties, their spread in a form and orientations. In this case, the spread in the inclusion forms can be conveniently realized with sorting all the inclusions by types depending on the form and including similarly-shaped inclusions into each type. At the same time, the form of all the inclusions of this type is assumed to be the same and equal to an average form of the inclusions of this type. Then, if separating the inclusions of the composite sample into n types, the formula (1) will be written as follows:

$$\boldsymbol{\varepsilon}^* = \left[\left(1 - \sum_{j=1}^n f_j\right)\varepsilon_m \mathbf{I} + \sum_{j=1}^n f_j \langle \boldsymbol{\kappa}^j \rangle\right] \times \left[\left(1 - \sum_{j=1}^n f_j\right)\mathbf{I} + \sum_{j=1}^n f_j \langle \boldsymbol{\lambda}^j \rangle\right]^{-1}. \quad (4)$$

where f_j is a volume portion of the inclusions of the j-type, $j = 1, \ldots, n$; $\langle \boldsymbol{\lambda}^j \rangle$, $\langle \boldsymbol{\kappa}^j \rangle$ are average values of the tensors $\boldsymbol{\lambda}$and $\boldsymbol{\kappa}$ by the inclusions of the j-the type. Since the form and the material characteristics of all the inclusions of this type are assumed to be the same, then averaging by the inclusions of this type means averaging by orientations of the inclusions of this type in a certain fixed system of coordinates xyz, which is related to this film sample. Let us select an axis z perpendicular to the film plane along a direction of propagation of the electromagnetic wave and the axes x, y perpendicular to each other in the film plane so that the system xyz is a right-handed one.

We relate each inclusion to the system of coordinates $\xi\eta\xi$, whose axes coincide with the axes of the respective ellipsoid: the axes ξ, η and ξ are directed along the semi-axes of the sizes a_1, a_2, a_3, respectively, wherein we will assume that a_3 is the least of the semi-axes. We also neglect a spread of the axes ξ of the inclusions from their ideal direction that coincides with the direction of the axis z. The directions of the axes ξ and η of the inclusions of each type will be assumed by us to be uniformly distributed in the film plane, i. e. in the plane xy. In this case, the tensor $\boldsymbol{\varepsilon}^*$ of the composite film will be uniaxial and diagonal in the system xyz, but its main components $\varepsilon_{11}^* = \varepsilon_{22}^* \neq \varepsilon_{33}^*$.

It can be shown (see the study [29]) that the magnitudes ε_{11}^*, ε_{22}^*, ε_{33}^* will not change when replacing distribution of orientations of the inclusions of each type with the axes ξ

Table 2. Aspect ratios and the volume portions of all the types of the aluminum inclusions in the composite film model

Inclusion type	$a_1 : a_2 : a_3$	f_j/f	Inclusion type	$a_1 : a_2 : a_3$	f_j/f	Inclusion type	$a_1 : a_2 : a_3$	f_j/f
1	3.8 : 3.8 : 1	0.0170	24	5.0 : 2.6 : 1	0.0182	47	1.64 : 6.1 : 1	0.0121
2	3.9 : 3.7 : 1	0.0170	25	2.6 : 5.0 : 1	0.0182	48	6.2 : 1.56 : 1	0.0121
3	3.7 : 3.9 : 1	0.0170	26	5.1 : 2.5 : 1	0.0186	49	1.56 : 6.2 : 1	0.0121
4	4.0 : 3.6 : 1	0.0170	27	2.5 : 5.1 : 1	0.0186	50	6.3 : 1.48 : 1	0.0121
5	3.6 : 4.0 : 1	0.0170	28	5.2 : 2.4 : 1	0.0186	51	1.48 : 6.3 : 1	0.0121
6	4.1 : 3.5 : 1	0.0170	29	2.4 : 5.2 : 1	0.0186	52	6.4 : 1.40 : 1	0.0121
7	3.5 : 4.1 : 1	0.0170	30	5.3 : 2.3 : 1	0.0179	53	1.40 : 6.4 : 1	0.0121
8	4.2 : 3.4 : 1	0.0170	31	2.3 : 5.3 : 1	0.0179	54	6.5 : 1.34 : 1	0.0121
9	3.4 : 4.2 : 1	0.0170	32	5.4 : 2.2 : 1	0.0170	55	1.34 : 6.5 : 1	0.0121
10	4.3 : 3.3 : 1	0.0170	33	2.2 : 5.4 : 1	0.0170	56	6.7 : 1.35 : 1	0.0119
11	3.3 : 4.3 : 1	0.0170	34	5.5 : 2.12 : 1	0.0156	57	1.35 : 6.7 : 1	0.0119
12	4.4 : 3.2 : 1	0.0170	35	2.12 : 5.5 : 1	0.0156	58	7.0 : 1.35 : 1	0.0112
13	3.2 : 4.4 : 1	0.0170	36	5.6 : 2.04 : 1	0.0147	59	1.35 : 7.0 : 1	0.0112
14	4.5 : 3.1 : 1	0.0172	37	2.04 : 5.6 : 1	0.0147	60	7.3 : 1.40 : 1	0.0107
15	3.1 : 4.5 : 1	0.0172	38	5.7 : 1.96 : 1	0.0137	61	1.40 : 7.3 : 1	0.0107
16	4.6 : 3.0 : 1	0.0172	39	1.96 : 5.7 : 1	0.0137	62	7.6 : 1.40 : 1	0.0105
17	3.0 : 4.6 : 1	0.0172	40	5.8 : 1.88 : 1	0.0133	63	1.40 : 7.6 : 1	0.0105
18	4.7 : 2.9 : 1	0.0172	41	1.88 : 5.8 : 1	0.0133	64	8.2 : 1.45 : 1	0.0102
19	2.9 : 4.7 : 1	0.0172	42	5.9 : 1.8 : 1	0.0128	65	1.45 : 8.2 : 1	0.0102
20	4.8 : 2.8 : 1	0.0177	43	1.8 : 5.9 : 1	0.0128	66	9.0 : 1.50 : 1	0.0088
21	2.8 : 4.8 : 1	0.0177	44	6.0 : 1.72 : 1	0.0123	67	1.50 : 9.0 : 1	0.0088
22	4.9 : 2.7 : 1	0.0179	45	1.72 : 6.0 : 1	0.0123	68	11 : 1.60 : 1	0.0058
23	2.7 : 4.9 : 1	0.0179	46	6.1 : 1.64 : 1	0.0121	69	1.60 : 11 : 1	0.0058

and η that are uniformly distributed in the plane xy with one, at which exactly a half of the inclusions of this type will have the axis ξ directed along the axis x and the other half — along the axis y (the axes ξ of all the inclusions are still directed along the axis z), Thus, technically, in order to calculate the tensor$\boldsymbol{\varepsilon}^*$, each type of the inclusions shaped as a general ellipsoid with the various values of the semi-axes a_1, a_2, a_3 with the axes ξ, η uniformly distributed in the plane xy can be replaced with two types of the inclusions with a fixed orientation and values of the semi-axes a_1, a_2, a_3 and a_2, a_1, a_3, respectively, wherein the volume portions of these new types of the inclusions will be equal to a half of the volume portion of the initial type of the inclusions.

Then, instead of the expression (4) we will have the following formula for calculating $\boldsymbol{\varepsilon}^*$:

$$\boldsymbol{\varepsilon}^* = \left[\left(1 - \sum_{j=1}^{n} f_j\right)\varepsilon_m \mathbf{I} + \sum_{j=1}^{n} f_j \boldsymbol{\kappa}^j\right] \times \left[\left(1 - \sum_{j=1}^{n} f_j\right)\mathbf{I} + \sum_{j=1}^{n} f_j \boldsymbol{\lambda}^j\right]^{-1}. \quad (5)$$

in which n and f_j designate a number of the new types of the inclusions and their volume portions, respectively. Due to the fact that the axes of the inclusions coincide with the axes of the system of coordinates xyz and the inclusions have scalar permittivity $\boldsymbol{\varepsilon} = \varepsilon\mathbf{I}$, the tensors $\boldsymbol{\lambda}^J$

and $\boldsymbol{\kappa}^j$ $(j = 1, \ldots, n)$ in the system xyz are diagonal and their main components

$$\lambda_i^{(j)} = \left(1 + \varepsilon_m^{-1} L_i^{(j)} (\varepsilon^{(j)} - \varepsilon_m)\right)^{-1}, \quad \kappa_i^{(j)} = \varepsilon^{(j)} \lambda_i^{(j)},$$
$$i = 1, 2, 3, \quad j = 1, \ldots, n, \tag{6}$$

where $L_i^{j)}$, $i = 1, 2, 3$ are the main components of the tensor of the geometrical factors of the inclusions of the j-th type with the semi-axes $a_1^{(j)}, a_2^{(j)}, a_3^{(j)}$, which are calculated by formulas that are similar to (3); $\varepsilon^{(j)}$ — permittivity of the inclusions of the j-type, whose value is corrected due to a size effect as a result of reduction of a mean free path of electron in a small metal particle. A dimensional correction is based on a Drude model in the following form [30]:

$$\varepsilon^{(j)}(\omega, \langle l \rangle^{(j)}) = \varepsilon_b(\omega) + \frac{\omega_p^2}{\omega(\omega + i\gamma_0)} - \frac{\omega_p^2}{\omega(\omega + i\gamma^{(j)})},$$
$$j = 1, \ldots, n, \tag{7}$$

where $\varepsilon_b(\omega)$ is permittivity of the bulk sample at the frequency ω; ω_p is a plasma frequency; γ_0 — an electron decay constant in the bulk sample of the material; $\gamma^{(j)} = \gamma_0 + (A v_F)/\langle l \rangle^{(j)}$ — an electron decay constant in the particle of the j-type, which is changed taking into account the size effect; v_F is an electron velocity on the Fermi surface; $\langle l \rangle^{(j)}$ is an average mean free path in the particle of j-type; A is a dimensionless parameter determined by details of a process of electron scattering by the particle surface, which is often assumed to be 1. Assuming that electrons are scattered from the inclusion boundary by a Lambert law, for $\langle l \rangle^{(j)}$ we have [31]:

$$\langle l \rangle^{(j)} = \frac{4V^{(j)}}{S^{(j)}}, \quad j = 1, \ldots, n, \tag{8}$$

where $V^{(j)}$ is a volume of the particle of the j-th type, $S^{(j)}$ is an area of its surface.

The main complex refractive indices $\tilde{n}_j^*$ and the main refractive indices n_j^* and the extinction coefficients k_j^* of the composite film are calculated by the formulas:

$$\tilde{n}_j^* = \sqrt{\varepsilon_j^*}, \quad n_j^* = \mathrm{Re}\sqrt{\varepsilon_j^*}, \quad k_j^* = \mathrm{Im}\sqrt{\varepsilon_j^*}, \quad j = 1, 2, 3. \tag{9}$$

At the same time, by virtue of uniaxiality of the tensor $\boldsymbol{\varepsilon}^*$ this composite film has axial symmetry of its optical properties: $n_1^* = n_2^* = n_\parallel^*$, $k_1^* = k_2^* = k_\parallel^*$, a subscript „$\parallel$“ designates a component that corresponds to the film plane.

Based on the formulas (5)–(9) and the matrix composite model with 69 types of the aluminum inclusions, we calculated the refractive index n_j^* and the extinction coefficient k_j^* of this composite film as well as its transmittance factor T at normal incidence of the electromagnetic wave. Dependences of the optical characteristics of amorphous SiO_2, aluminum and values of the Drude model's parameters for aluminum ($v_F = 2.03 \cdot 10^6$ m/s, $\hbar\gamma_0 \approx 0.129$ eV, $\hbar\omega \approx 12.7$ eV) were taken from the study [32]. The

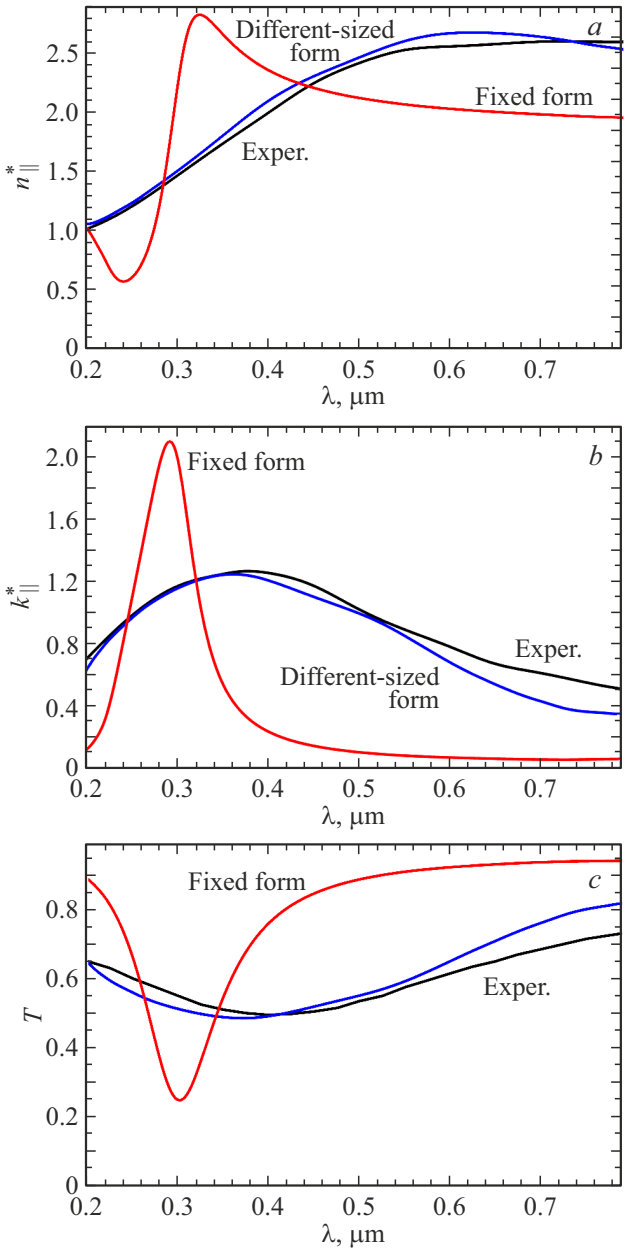

Figure 9. Spectral dependences of the refractive index (a), the extinction coefficient (b) and the transmittance factor (c) of the composite film with the SiO_2 matrix and the aluminum inclusions, which are obtained by ellipsometric measurements (the black curves) and the calculations by the generalized MG approximation with taking into account the spread in the inclusion forms (the blue curves) and with the fixed inclusion form (the red curves).

aspect ratios of the inclusions of all the types and their relative volume portions are provided in Table 2. The full volume portion of the inclusions $f = 0.165$, the size of the semi-axis a_3 for all the inclusions is 2.25 nm. In the calculations, the thickness of the composite film was assumed to be 12.5 nm.

Figure 9 shows results of calculations of n, k and T, respectively. The data of n, k and T for the selected

sample #2, which are experimentally obtained by meas of ellipsometric measurements, are shown in Figure 9 by the black curves. It is shown by calculations using the MG approximation for the case when the Al nanoparticle array consists of form- and size-identical flattened spheroids with the aspect ratio of 3.8 : 3.8 : 1 and the volume portion $f = 0.1$ that a well-pronounced LSPR shall be at the wavelength of ~ 300 nm. At the same time, in this case the calculation results demonstrate a significant deviation (the red curves) from the experiment (the black curves).

The experimentally-obtained dependences (the black curves) are shaped as highly smoothed curves, the maximum of the extinction coefficient (Figure 9, *b*) and the minimum of the transmittance factor (Figure 9, *c*) of the composite film are very heavily smeared and a rise of the refractive index (Figure 9, *a*) in the spectral range that includes plasmon resonances on the surface of the composite inclusions, is very smooth. The optical characteristics are calculated by the model with the 69 types of the inclusions by means of MG to show that this smearing of the dependences can be explained exactly by the large spread of the inclusions in the form. The calculated blue curves in Figure 9 are in good compliance with the experimental ones, and for the refractive index the calculations by this model provide somewhat overestimated values within the interval $0.32-0.74\,\mu$m, while for the extinction coefficient they provide somewhat underestimated values within the interval $0.38-0.8\,\mu$m, wherein the interval $0.58-0.74\,\mu$m exhibits a somewhat sharper drop of the calculated dependence as compared to the experimental one. The calculated dependence of the film's transmittance factor within the range $0.2-0.4\,\mu$m provides somewhat underestimated (by 8%, at most) values, while within the range $0.4-0.58\,\mu$m it provides close, somewhat overestimated values, wherein within the range $0.58-0.8\,\mu$m it provides values of the transmittance factor, which are overestimated by 5–12% as compared to the experimental values.

Thus, it can be concluded that the spectral dependences of the optical characteristics of the produced Al nanoparticle arrays covered with the SiO_2 layer are primarily smeared by the large spread of the aluminum inclusions in the forms. It can be also concluded that the method based on the generalized MG approximation (1) and the matrix composite model with several types of the inclusions can be used to adequately predict the optical properties of nanocomposites with a dielectric matrix and metal inclusions provided that the sizes of the inclusions are small as compared to a wavelength of electromagnetic radiation and components of this medium have not magnetic properties.

4. Conclusion

Thus, it is demonstrated in this article that it is possible to form the aluminum nanoparticle arrays with a controllable average nanoparticle size within the range from several nanometers to ~ 80 nm by vacuum-thermal deposition. At the same time, the nanoparticle size linearly depends on the number of deposited Al. Irrespective of the size, the Al nanoparticles in the array have a flattened form, when the height of the nanoparticles is in 1.9–2.5 times less than the planar size. It was detected that the nanoparticles have a face-centered crystal lattice and lattice parameters that were typical for bulk Al. The experimental data obtained by ellipsometry and the simulation results were compared to show that the spectral optical characteristics of the aluminum nanoparticle array covered with the SiO_2 layer decisively vary due to heterogeneity of the form of the Al nanoparticles in the array. Good compliance of the simulation results and the experimental optical characteristics of the studied material shows that the method based on the generalized MG approximation and the matrix composite model with several types of the inclusions can be used to predict the optical properties of nano-composites with a dielectric matrix and metal inclusions provided that the there are the particles of a small size as compared to a wavelength of electromagnetic radiation and components of this medium have not magnetic properties.

Funding

The study was performed under the state assignment (Agreement FSMR-2025-0006).

Conflict of interest

The authors declare that they have no conflict of interest.

References

[1] A. Raj, R.K. Thomas. Optical and molecular physics. Apple Academic Press. (2021). Vol. 1, p. 43.
[2] V.I. Balykin, P.N. Melent'ev. UFN (in Russian). **188**, *2*, 143 (2018).
[3] S.V. Dubkov, A.I. Savitskiy, A.Yu. Trifonov, G.S. Yeritsyan, Yu.P. Shaman, E.P. Kitsyuk, A. Tarasov, O. Shtyka, R. Ciesielski, D.G. Gromov. Opt. Mater. X **7**, 100055 (2020).
[4] D.G. Gromov, S.V. Dubkov, A.I. Savitskiy, Yu.P. Shaman, A.A. Polokhin, I.A. Belogorokhov, A.Yu. Trifonov. Appl. Surf. Sci. **489**, 701 (2019).
[5] K. Kneipp. Phys. Today **60**, *11*, 40 (2007).
[6] T.P. Araujo, J. Quiroz, E.C.M. Barbosa, P.H.C. Camargo. Curr. Opin. Colloid Interface Sci. **39**, 110 (2019).
[7] H. Lee, H. Lee, J.Y. Park. Nano Lett. **19**, *2*, 891 (2019).
[8] C. Yao, J. Lin, L. Li, K. Jiang, J. Sun, J. Wu. Phys. Status Solidi A **218**, *9*, 2000737 (2021).
[9] F. Temerov, K. Pham, P. Juuti, J.M. Mäkelä, J.M. Grachova, S. Kumar, S. Eslava, J. Saarinen. ACS Appl. Mater. Interfaces **12**, *37*, 41200 (2020).
[10] Y. Hattori, S.G. Álvarez, J. Meng, K. Zheng, J. Sá. ACS Appl. Nano Mater. **4**, *2*, 2052 (2021).
[11] R. Li, D. Wang, W. Wang, X. Ao, G.C. Schaz, R. Schaller, T.W. Odom. J. Opt. Soc. Am. B **36**, *7*, 104 (2019).
[12] A. Loiseau, V. Asila, G. Boitel-Aullen, M. Lam, M. Salmain, S. Boujday. Biosensors **9**, *2*, 78 (2019).

[13] N.A. Brazhe, A.B. Evlyukhin, E.A. Goodilin, A.A. Semenova, S.M. Novikov, S.I. Bozhevolniy, B.N. Chichkov, A.S. Sarycheva, A.A. Baizhumanov, E.I. Nikelshparg, L.I. Deev, E.G. Maksimov, G.V. Maksimov, O. Sosnovtseva. Sci. Rep. **5**, *1*, 13793 (2015).
[14] U. Boda, J. Strandberg, J. Eriksson, X. Liu, V. Beni, K. Tybrandt. ACS Appl. Mater. Interfaces **15**, *9*, 12372 (2023).
[15] A.E. Ershov, V.S. Gerasimov, R.G. Bikbaev, S.P. Polyutov, S.V. Karpov. J. Quant. Spectrosc. Radiat. Transf. **248**, 106961 (2020).
[16] M.W. Knight, N.S. King, L. Liu, H.O. Everitt, P. Nordlander, N.J. Halas. ACS Nano **8**, *1*, 834 (2014).
[17] X. Liu, A.W. Bruch, H.X. Tang. Adv. Opt. Photonics. **15**, *1*, 236 (2023).
[18] D. Han, S. Deng, T. Ye, Y. Wei. Microsyst. Nanoeng. **9**, *1*, 40 (2023).
[19] C.K. Chang, H.Y. Chien. Opt. Laser Technol. **174**, 110653 (2024).
[20] E.S. Kim, Y.M. Kim, K.C. Choi. Plasmonics **11**, *5*, 1337 (2016).
[21] K. Yang, X. Yao, B. Liu, B. Ren. Adv. Mater. **33**, *50*, 2007988 (2021).
[22] A.N. Shipway, E. Katz, I. Willner. Chem. Phys. Chem. **1**, *1*, 18 (2000).
[23] Ch.Z. Wang, K. Huang, N. Gao, Zh.M. Wu, J.Y. Kang. Appl. Mech. Mater. **621**, 65 (2014).
[24] D.G. Gromov, L.M. Pavlova, A.I. Savitskiy, A.Yu. Trifonov. Phys. Solid State **57**, *1*, 173 (2015).
[25] D.G. Gromov, L.M. Pavlova, A.I. Savitskiy, A.Yu. Trifonov. Appl. Phys. A. **118**, *4*, 1297 (2015).
[26] T.S. Grishin, L.S. Volkova, A.A. Dudin, G.A. Medenkov, D.V. Novikov, S.V. Dubkov, D.G. Gromov. Opt. Mater. **167**, 117260 (2025).
[27] K. Boren, D. Khafmen. Pogloschenie i rasseyanie sveta malymi chastitsami. Mir, M. (1986). 660 s. (in Russian).
[28] I.V. Lavrov. Izvestiya vuzov. Elektronika **28**, *4*, 403 (2023). (in Russian).
[29] I.V. Lavrov. Vychislenie effektivnykh dielektricheskikh i provodyashchikh kharakteristik sluchaino-neodnorodnykh teksturirovannykh sred: diss. k.f.-m. nauk. M.: MIET, 2010. 167 s. (in Russian).
[30] W.T. Doyle. Phys. Rev. B. **39**, *14*, 9852 (1989).
[31] E.A. Coronado, G.C. Schatz. J. Chem. Phys. **119**, 3926 (2003).
[32] E.D. Palik. Handbook of Optical Constants of Solids. Acad. Press, Orlando. (1985). Vol. 3, 804 p.

Translated by M.Shevelev